Attractor dimension of time-averaged climate observables: insights from a low-order ocean-atmosphere model

Davide Faranda, Gabriele Messori, Stéphane Vannitsem

Attractor dimension of time-averaged climate observables: insights from a low-order ocean-atmosphere model

D. Faranda[1,2], Gabriele Messori[3,1], Stéphane Vannitsem[4]

[1]LSCE-IPSL, CEA Saclay l'Orme des Merisiers, CNRS UMR 8212 CEA-CNRS-UVSQ, Université Paris-Saclay, 91191 Gif-sur-Yvette, France.

[2]London Mathematical Laboratory, 14 Buckingham Street, London, WC2N 6DF, UK

[3]Department of Meteorology and Bolin Centre for Climate Research, Stockholm University, 106 91, Stockholm, Sweden

[4]Royal Meteorological Institute of Belgium, Bruxelles, Belgium

Corresponding author: D. Faranda, davide.faranda@lsce.ipsl.fr

Abstract

The ocean and atmosphere have very different characteristic timescales and display a rich range of interactions. Here, we investigate the sensitivity of the dynamical properties of the coupled atmosphere-ocean system to time-averaging. We base our analysis on a conceptual model of the atmosphere-ocean dynamics which allows us to compute the attractor properties for different coupling coefficients and averaging time-scales. When the averaging time is increased, the local dimension shows a non-monotonic behaviour for short averaging times, but ultimately decreases for windows longer than 1 year. The analysis of daily, monthly and annual instrumental and reconstructed indices of oceanic and atmospheric circulation supports our results. This has important implications for the analysis and interpretation of long climate timeseries with a low temporal resolution, but also on the possible convergence of climate observables for long time-averages toward attractors close to hyperbolicity.

1 Introduction

The climate system is a complex system characterised by turbulent dynamics. The time-energy spectra of instrumental and proxy climate data show a rich structure with energy cascades from timescales of millions of years to a few seconds and no spectral gaps [*Lovejoy et al.*, 2001]. Moreover, atmospheric and oceanic motions feature specific characteristics which differentiate them from the homogeneous and isotropic turbulence of Kolmogorov [*Pouquet and Marino*, 2013]. Indeed, the rotation and stratification effects allow for an inverse energy cascade contributing to large-scale motions, such as the atmospheric planetary waves and ocean currents. The different components of the climate system - each with their own complex dynamics - further show a broad range of interactions. In this study we will specifically focus on the interplay between the ocean and atmosphere. The former has slow characteristics timescales (up to thousands of years), while the latter has a swifter temporal evolution, with synoptic-scale features typically evolving over periods of days [*Pedlosky*, 2013]. These fast timescales limit our ability to predict the future evolution of atmospheric dynamics: indeed, *Lorenz* [1969, 1982] and *Dalcher and Kalnay* [1987] postulated a limit of mid-latitude weather predictability at 10-15 days. However, the ocean's slow variability provides a possible predictability pathway beyond this range [*Palmer and Anderson*, 1994; *Baehr et al.*, 2015; *Vannitsem and Ghil*, 2017]. This makes the study of the ocean's low frequency variability (LFV) and

its coupling with the atmosphere a topic of considerable scientific and practical interest.

The most famous example of ocean-led predictability is the alternance of El-Nino and La-Nina events and their effects on large-scale precipitation and temperatures. This phenomenon has provided some of the earliest indications of the feasibility of annual and longer forecasts [*Cane et al.*, 1986]. However, extracting the full predictability potential inherent to LFV features on longer timescales remains a challenge. Long instrumental time-series are scarce, and even reanalysis products only provide well-constrained data over the past few decades. Long-term reconstructions of coupled ocean/atmosphere variability must therefore rely on model simulations, documentary evidence or proxy data. The latter typically provide a time series representative of some feature of oceanic and/or atmospheric circulation on a regional or larger scale, with a time resolution of seasons to decades or longer [*Bond et al.*, 2001; *Vinther et al.*, 2010]. This type of data is essential to verify that the coupled dynamics generated by climate models are compatible with those found in real world.

An important question is whether it is possible to quantify the impact of the averaging procedure implicit in proxy records when performing such comparisons. In this paper, we address this question from a theoretical angle by using a conceptual coupled ocean-atmosphere model and investigating its dynamical properties. We apply dynamical systems theory to measure the dimensionality of the system, and compare the results for model output with a high temporal resolution versus a degraded dataset where the system is known only through long-term averages. This allows us to objectively quantify the modifications induced by the averaging. We conclude by applying our approach to a number of instrumental and reconstructed indices of large-scale climate modes and discussing the implications of our results for the general analysis of climate data.

2 A dynamical systems approach

Determining the attractor properties of complex systems has been a long-standing challenge in the field of dynamical systems theory. However, recent theoretical advances in our understanding of the limiting distribution of Poincaré recurrences now enable us to compute both mean and instantaneous (in time, and hence local in phase space) dynamical properties of complex systems. The key finding is that, under suitable rescal-

ing, the probability p of entering a ball in phase space centred on ζ with a radius r for chaotic attractors obeys a generalized Pareto distribution [*Freitas et al.*, 2010; *Faranda et al.*, 2011; *Lucarini et al.*, 2012, 2016]. In order to compute such probability, we first calculate the series of distances $dist(\zeta, x(t))$ between the point on the attractor ζ and all other points $x(t)$ on the trajectory. We then put a logarithmic weight on the time series of the distance to increase the discrimination of small values of $dist(\zeta, x(t))$, which correspond to large values of $g(x(t))$:

$$g(x(t)) = -\log(dist(\zeta, x(t))).$$

The probability of entering a ball of radius r centred on ζ can now be expressed as the probability p of exceeding a threshold q of the distribution of $g(x(t))$. In the limit of an infinitely long trajectory, such probability is the exponential member of the generalized Pareto distribution:

$$p = \Pr(g(x(t)) > q, \zeta) \simeq \exp(-[x - \mu(\zeta)]/\beta(\zeta))$$

whose parameters μ and σ are a function of the point ζ chosen on the attractor. Remarkably, $\sigma = 1/d(\zeta)$, where $d(\zeta)$ is the local dimension around the point ζ. The attractor dimension $\langle d \rangle$ can then be obtained by averaging d for a sufficiently large sample of points ζ_i on the attractor. Here, we use the quantile 0.98 of the series $g(x(t))$ to determine q. We have checked the stability of the results against reasonable changes in the quantile. The universality of the convergence law implies that the above is akin to a central limit theorem of Poincaré recurrences. For further details, the reader is referred to *Lucarini et al.* [2016]. The above approach has been successfully used to describe the evolution of sea-level pressure [*Faranda et al.*, 2017a] and geopotential height fields [*Messori et al.*, 2017] over the North Atlantic, as well as sea-level pressure, temperature and precipitation fields at hemispheric scale [*Faranda et al.*, 2017b].

3 Data and Model Specifications

3.1 A Conceptual Atmosphere-Ocean Coupled Model

The coupled ocean-atmosphere model we use here is the same as described by *Vannitsem* [2015]. The atmospheric component is based on the vorticity equations of a two-

layer, quasi-geostrophic flow defined on a β-plane, supplemented with a thermodynamic equation for the temperature at the interface between the two atmospheric layers. The ocean component is based on the reduced-gravity, quasi-geostrophic shallow-water model with the same first order approximation of the Coriolis parameter. The oceanic temperature is considered as a passive scalar transported by the ocean currents, but it displays strong interactions with the atmospheric temperature through radiative and heat exchanges. A time-dependent radiative forcing mimicks the annual radiative input coming from the Sun at midlatitudes. A low-order model version is built based on truncating the Fourier expansion of the fields at the minimal number of modes that are believed to capture key features of the observed large scale dynamics of both the ocean and the atmosphere. The truncation leads to 20 ordinary differential equations for the atmospheric variables, 8 equations for the ocean transport variables, 6 equations for the temperature anomaly within the ocean, and 2 additional equations for the spatially averaged temperatures in the atmosphere and the ocean. The parameter values used are the same as in Figure 3 of *Vannitsem* [2015], except that here we test a different range of values of the friction coefficient between the ocean and the atmosphere, namely C. Specifically, we consider 4 different runs, coined CD0002, CD0005, CD0007 and CD0008, corresponding to 4 different values of the friction coefficient between the ocean and the atmosphere, namely C=0.002, 0.005, 0.007 and 0.008 $\mathrm{kgm^{-2}s^{-1}}$, respectively. The last two runs display LFV, while the first two do not. The lengths of the series is such that we can retain 10000 time-steps for all averaging windows in what follows.

3.2 Data

In addition to output from an idealised model, we also analyse real-world timeseries at different temporal resolutions. Specifically, we use daily NINO3 data provided by the NOAA climate prediction center [*Barnston and Livezey*, 1987; *Reynolds et al.*, 2007] over the period 01 Jan 1981 - 28 Feb 2018, monthly NINO3 data over 1854 to 2016 provided by [*Huang et al.*, 2017] and a yearly NINO3 dataset over the period 1049-1995 provided by *Mann et al.* [2009]. We further analyse daily NAO data provided by the NOAA climate prediction center [*Barnston and Livezey*, 1987; *Reynolds et al.*, 2007] over the period 01 Jan 1981 - 28 Feb 2018, monthly NAO data over 1854 to 2016 provided by [*Jones et al.*, 1997] and yearly data over the period 1049-1995 [*Trouet et al.*, 2009].

4 Dynamical Implications of Time-Averaging

We begin by analysing the dependence of the phase portraits on the time-averaging of model output. In order to depict this we have to choose 3 of the 36 modes of the model to represent the attractor on a Poincaré section. We choose modes $\psi_{o,2}$, $\theta_{o,2}$ and $\psi_{a,1}$ (Figure 1). These three modes are the dominant modes of the coupled ocean-atmosphere dynamics as discussed in detail in *Vannitsem et al.* [2015]. We consider a run with no LFV (C=0.002, Figure 1 a, c, e, g) and a run with a marked LFV (C=0.007, Figure 1 b, d, f, h). The colourscales show the values of the local dimension d (for readability each panel has a different colourscale). The effect of averaging depends both on the chosen time-window and on the coupling. The daily portraits show quasi-periodic cycles, associated with the annual cycle present in the system, in both simulations (Figure 1 a, b). These are partly destroyed by the monthly averaging (Figure 1 c, d). Longer time-averaging rapidly smooths all structures in the phase portraits of the no-LFV run (Figure 1 e, g), so that the Poincaré section looks like that of a noisy fixed point in 3 dimensions. For the LFV run, the slow signal associated with the ocean dynamics survives the averaging procedures, and is still evident under an 8-year averaging. We further note that at sub-annual time scales (Figure 1 a, b, c, d), the local dimension is in general higher during the winter period, i.e. when $\psi_{a,1}$ – characterizing the amplitude of the atmospheric zonal flow – displays high values. We will come back to this point in the next section.

A more quantitative analysis of the changes in the attractor properties under averaging is reported in Figures 2 and 3, which present the mean values and distributions of d. The first remarkable feature is the non-monotonic behaviour of the dimension with the averaging window. A naive hypothesis would be that, independently of the coupling, one might observe a decrease of the dimension with increasing time-averaging. However, this is only true for averaging periods larger or equal to 1 year, for which the seasonal cycle is averaged out. Indeed, all four simulations analysed here show non-monotonic behaviour for shorter averaging times. This feature reveals that the filtering through averaging tends to modify the frequency of specific categories of local dimensions. The analysis of the distributions of d, shown in Figure 3, provides further insights on this behaviour. Taking C=0.002 as example, one can see a clear shift of the distribution toward larger values in going from daily to monthly values.

On the contrary, averaging beyond 1 year time-scales suppresses the extreme d values in the tails of the distributions, which corresponds to a smoothing of the variability of the dimension, thus lowering $\langle d \rangle$. This is particularly evident for the case of C=0.007 and C=0.008 (LFV runs) and should be expected since there is a smoothing of the variability on the attractor (Figure 1 b, d, f, h). This smoothing removes specific frequencies in the dynamics, as discussed in details in *Nicolis and Nicolis* [1995]; *Vannitsem and Nicolis* [1995, 1998], and also reduces the local variability of the instability properties of the flow. Another interesting result is that at monthly and seasonal scales the distributions of d display a double peak for runs both with and without LFV (Figure 4). This double peak is associated with the seasonal variability; there is a dominance of large d in Winter and low d in Summer. For instance for C=0.005, there is a maximum around $d = 8$ for the winter conditions and $d = 4$ for summer conditions (Figure 4) . To interpret this feature one must recall that the large-scale winter dynamics in the mid-latitudes is driven by a larger gradient of equator-to-pole radiative input than in summer [*Goosse*, 2015; *Vannitsem*, 2015, 2017]. This has strong implications for the instability properties of the flow [*Buizza and Palmer*, 1995]. This is also a property of the coupled ocean-atmosphere model used here, which displays lower averaged local Lyapunov exponents (and averaged local Lyapunov dimensions) in Summer than in Winter [*Vannitsem*, 2017]. The technique we adopt here succesfully captures this increase in the complexity of the dynamics. The distributions further highlight the fact that, in some cases, the average of d remains roughly constant but the positive tails of the distributions change radically. This suggests that a decrease in $\langle d \rangle$ due to averaging might change little in the system's ground state while altering the configurations with the largest number of degrees of freedom. Table 1 reports the values of the first four moments of the distribution of d for all C and averaging times.

One can further wonder whether $\langle d \rangle$ are determined predominantly by the oceanic or the atmospheric modes. To do this, we compute the local dimensions of the oceanic and atmospheric components separately. The results are shown in Figure 5 for different averaging periods. Except for the C=0.007 case, the atmospheric modes alone return almost the same value of the total dimension as the joint calculation. The analysis of the ocean variables instead gives a lower dimension. This interesting feature likely reflects the fact that, although the ocean variables are coupled to the atmosphere, they only retains part of the complex structure of the system, in particular for the low values of C.

In our view, this results from the fact that the dynamics in the ocean is only "weakly" driven by the chaotic variability present in the atmosphere for small values of C due to the large inertia of the ocean that integrates the atmospheric forcing on long time scales. For large values of C, LFV develops and this effect is considerably weakened; variables from both components then provide similar results. However, the behavior observed for $C = 0.007$ is still slightly non-monotonic because this run still gives a chaotic attractor, whereas the run $C = 0.008$ provide a quasi-periodic flow.

5 Implications for Ocean-Atmosphere Coupling and conclusions

In the present study we have investigated the effects of time averaging on the ocean-atmosphere system as represented by a conceptual coupled model. The impact of averaging is quantified in terms of changes in the attractor properties of the system. When the averaging time is increased, the local dimension shows a non-monotonic behaviour for short averaging times, but ultimately decreases for windows longer than 1 year. For these averaging windows, the distribution of the local dimension becomes closer to Gaussian and the variability decreases. This corresponds to a progressive smoothing of the attractor. Time-averaging therefore has profound and sometimes counter-intuitive implications for the dynamical characteristics of climate data. Our results also suggest that, on longer time scales, the climate dynamics is smoother and closer to that of homogenous, hyperbolic systems.

It is however necessary to verify whether the results from the idealised model presented above find a match in real-world data. Here, we repeat our analysis for El Nino-Southern Oscillation Nino3 and North Atlantic Oscillation (NAO) indices. As a caveat, we note that this analysis has an important difference from that of the full coupled model. Indeed, the NAO and Nino3 indices do not represent the full climate attractor whereas they can be thought of as a projection (a special Poincaré section) of the full dynamics. In this sense the analysis can still inform us on numerous aspects of the system (see for example *Faranda et al.* [2017c] for a similar argument on the Von Karmann turbulent swirling flow). A separate problem to consider is the length of the time series, as our method for computing the local dimensions is dependent on processing a sufficiently long series. The shortest timeseries we analyse are the yearly ones, for which we only dispose of 947 years; we therefore perform two different computations of the dimension: i) for each dataset we use the complete timeseries, ii) for each dataset we only use 947 data

points. This provides some indication of the robustness of our conclusions. The results are reported in Figure 6. The top panels show the boxplot of the local dimension distributions when all the data are considered, whereas the lower panel presents the average dimension for the two cases described. The analysis of the boxplots suggest that the extremes of d change with the time scale considered. For the yearly time series, we obtain values of d up to 10. This may seem nonphysical since we are only analyzing two time series but, following again *Faranda et al.* [2017c], can be understood by considering the role of small scale turbulence in increasing the effective dimension of the attractor. Sampling issues may be discarded because both the full and reduced datasets show comparable relative changes between the different temporal resolutions. Finally the non-monotonic behavior of the average dimension for the climate indices follows the one found in the coupled model. We therefore conclude that the inferences drawn from the conceptual model provide valuable insights into the behaviour of real-world climate data and should be considered when performing dynamical analyses of data with low temporal resolutions. It is worth performing further analysis in more sophisticated climate models in order to clarify in particular the increase of variability of the local dimension found in Figure 6. For that, very long (historical) runs should be considered in order to have enough data for the extreme value analysis, provided that climate models can correctly reproduce the internal variability of the climate system.

6 Acknowledgments

D. Faranda and G. Messori were supported by ERC grant No. 338965. The work of Stéphane Vannitsem is partly supported by the Belgian Federal Science Policy under contract BR/165/A2/Mass2Ant. G. Messori was also supported by the Swedish Research Council under contract: 2016-03724

References

Baehr, J., K. Fröhlich, M. Botzet, D. I. Domeisen, L. Kornblueh, D. Notz, R. Piontek, H. Pohlmann, S. Tietsche, and W. A. Mueller (2015), The prediction of surface temperature in the new seasonal prediction system based on the mpi-esm coupled climate model, *Climate Dynamics*, *44*(9-10), 2723–2735.

Barnston, A. G., and R. E. Livezey (1987), Classification, seasonality and persistence of low-frequency atmospheric circulation patterns, *Monthly weather review*,

115(6), 1083–1126.

Bond, G., B. Kromer, J. Beer, R. Muscheler, M. N. Evans, W. Showers, S. Hoffmann, R. Lotti-Bond, I. Hajdas, and G. Bonani (2001), Persistent solar influence on north atlantic climate during the holocene, *Science*, *294*(5549), 2130–2136.

Buizza, R., and T. Palmer (1995), The singular-vector structure of the atmospheric global circulation, *Journal of the Atmospheric Sciences*, *52*(9), 1434–1456.

Cane, M. A., S. E. Zebiak, and S. C. Dolan (1986), Experimental forecasts of el nino, *Nature*, *321*(6073), 827.

Dalcher, A., and E. Kalnay (1987), Error growth and predictability in operational ecmwf forecasts, *Tellus A: Dynamic Meteorology and Oceanography*, *39*(5), 474–491.

Faranda, D., V. Lucarini, G. Turchetti, and S. Vaienti (2011), Numerical convergence of the block-maxima approach to the generalized extreme value distribution, *Journal of statistical physics*, *145*(5), 1156–1180.

Faranda, D., G. Messori, and P. Yiou (2017a), Dynamical proxies of north atlantic predictability and extremes, *Scientific reports*, *7*, 41,278.

Faranda, D., G. Messori, M. C. Alvarez-Castro, and P. Yiou (2017b), Dynamical properties and extremes of northern hemisphere climate fields over the past 60 years, *Nonlinear Processes in Geophysics*, *24*(4), 713.

Faranda, D., Y. Sato, B. Saint-Michel, C. Wiertel, V. Padilla, B. Dubrulle, and F. Daviaud (2017c), Stochastic chaos in a turbulent swirling flow, *Physical review letters*, *119*(1), 014,502.

Freitas, A. C. M., J. M. Freitas, and M. Todd (2010), Hitting time statistics and extreme value theory, *Probability Theory and Related Fields*, *147*(3-4), 675–710.

Goosse, H. (2015), *Climate System Dynamics and Modeling*, Cambridge University Press.

Huang, B., P. W. Thorne, V. F. Banzon, T. Boyer, G. Chepurin, J. H. Lawrimore, M. J. Menne, T. M. Smith, R. S. Vose, and H.-M. Zhang (2017), Extended reconstructed sea surface temperature, version 5 (ersstv5): upgrades, validations, and intercomparisons, *Journal of Climate*, *30*(20), 8179–8205.

Jones, P., T. Jonsson, and D. Wheeler (1997), Extension to the north atlantic oscillation using early instrumental pressure observations from gibraltar and southwest iceland, *International Journal of climatology*, *17*(13), 1433–1450.

Lorenz, E. (1982), Atmospheric predictability experiments with a large numerical model, *Tellus*, *34*(6), 505–513.

Lorenz, E. N. (1969), The predictability of a flow which possesses many scales of motion, *Tellus*, *21*(3), 289–307.

Lovejoy, S., D. Schertzer, and J. Stanway (2001), Direct evidence of multifractal atmospheric cascades from planetary scales down to 1 km, *Physical review letters*, *86*(22), 5200.

Lucarini, V., D. Faranda, and J. Wouters (2012), Universal behaviour of extreme value statistics for selected observables of dynamical systems, *Journal of statistical physics*, *147*(1), 63–73.

Lucarini, V., D. Faranda, A. C. M. Freitas, J. M. Freitas, H. Mark, K. Tobias, M. Nicol, M. Todd, and S. Vaienti (2016), Extremes and recurrence in dynamical systems.

Mann, M. E., Z. Zhang, S. Rutherford, R. S. Bradley, M. K. Hughes, D. Shindell, C. Ammann, G. Faluvegi, and F. Ni (2009), Global signatures and dynamical origins of the little ice age and medieval climate anomaly, *Science*, *326*(5957), 1256–1260.

Messori, G., R. Caballero, and D. Faranda (2017), A dynamical systems approach to studying midlatitude weather extremes, *Geophysical Research Letters*, *44*(7), 3346–3354.

Nicolis, C., and G. Nicolis (1995), From short-scale atmospheric variability to global climate dynamics: toward a systematic theory of averaging, *Journal of the atmospheric sciences*, *52*(11), 1903–1913.

Palmer, T. N., and D. L. Anderson (1994), The prospects for seasonal forecasting–a review paper, *Quarterly Journal of the Royal Meteorological Society*, *120*(518), 755–793.

Pedlosky, J. (2013), *Geophysical fluid dynamics*, Springer Science & Business Media.

Pouquet, A., and R. Marino (2013), Geophysical turbulence and the duality of the energy flow across scales, *Physical review letters*, *111*(23), 234,501.

Reynolds, R. W., T. M. Smith, C. Liu, D. B. Chelton, K. S. Casey, and M. G. Schlax (2007), Daily high-resolution-blended analyses for sea surface temperature, *Journal of Climate*, *20*(22), 5473–5496.

Trouet, V., J. Esper, N. E. Graham, A. Baker, J. D. Scourse, and D. C. Frank (2009), Persistent positive north atlantic oscillation mode dominated the medieval climate anomaly, *science*, *324*(5923), 78–80.

Vannitsem, S. (2015), The role of the ocean mixed layer on the development of the north atlantic oscillation: A dynamical system's perspective, *Geophysical Research Letters*, *42*(20), 8615–8623.

Vannitsem, S. (2017), Predictability of large-scale atmospheric motions: Lyapunov exponents and error dynamics, *Chaos: An Interdisciplinary Journal of Nonlinear Science*, *27*(3), 032,101.

Vannitsem, S., and M. Ghil (2017), Evidence of coupling in ocean-atmosphere dynamics over the north atlantic, *Geophysical Research Letters*, *44*(4), 2016–2026.

Vannitsem, S., and V. Lucarini (2016), Statistical and dynamical properties of covariant lyapunov vectors in a coupled atmosphere-ocean modelmultiscale effects, geometric degeneracy, and error dynamics, *Journal of Physics A: Mathematical and Theoretical*, *49*(22), 224,001.

Vannitsem, S., and C. Nicolis (1995), Dynamics of fine scale variables versus averaged observables in a simplified thermal convection model, *Journal of Geophysical Research: Atmospheres*, *100*(D8), 16,367–16,375.

Vannitsem, S., and C. Nicolis (1998), Dynamics of fine-scale variables versus averaged observables in a t21l3 quasi-geostrophic model, *Quarterly Journal of the Royal Meteorological Society*, *124*(551), 2201–2226.

Vannitsem, S., J. Demaeyer, L. De Cruz, and M. Ghil (2015), Low-frequency variability and heat transport in a low-order nonlinear coupled ocean–atmosphere model, *Physica D: Nonlinear Phenomena*, *309*, 71–85.

Vinther, B. M., P. Jones, K. Briffa, H. Clausen, K. Andersen, D. Dahl-Jensen, and S. Johnsen (2010), Climatic signals in multiple highly resolved stable isotope records from greenland, *Quaternary Science Reviews*, *29*(3), 522–538.

Table 1. Moments of the distributions of d for different C and averaging times.

	C=0.002				C=0.005				C=0.007				C=0.008			
	year	seas	month	day	year	seas	month	day	year	seas	month	day	year	seas	month	day
median	8.10	7.50	8.09	5.78	7.81	6.04	6.50	5.57	1.98	1.87	2.95	3.56	0.92	2.04	2.81	2.42
std	1.19	2.33	2.33	1.84	1.27	1.53	2.97	2.47	0.62	0.78	1.49	3.8	0.11	0.64	0.99	1.16
skewness	0.31	0.88	1.19	1.55	0.28	0.50	0.59	2.5	1.19	1.68	1.47	2.67	3.09	1.66	1.10	2.21
kurtosis	3.31	3.98	4.87	6.61	3.45	3.95	3.41	12.34	4.67	7.71	5.98	12.55	23.27	13.24	5.43	10.38

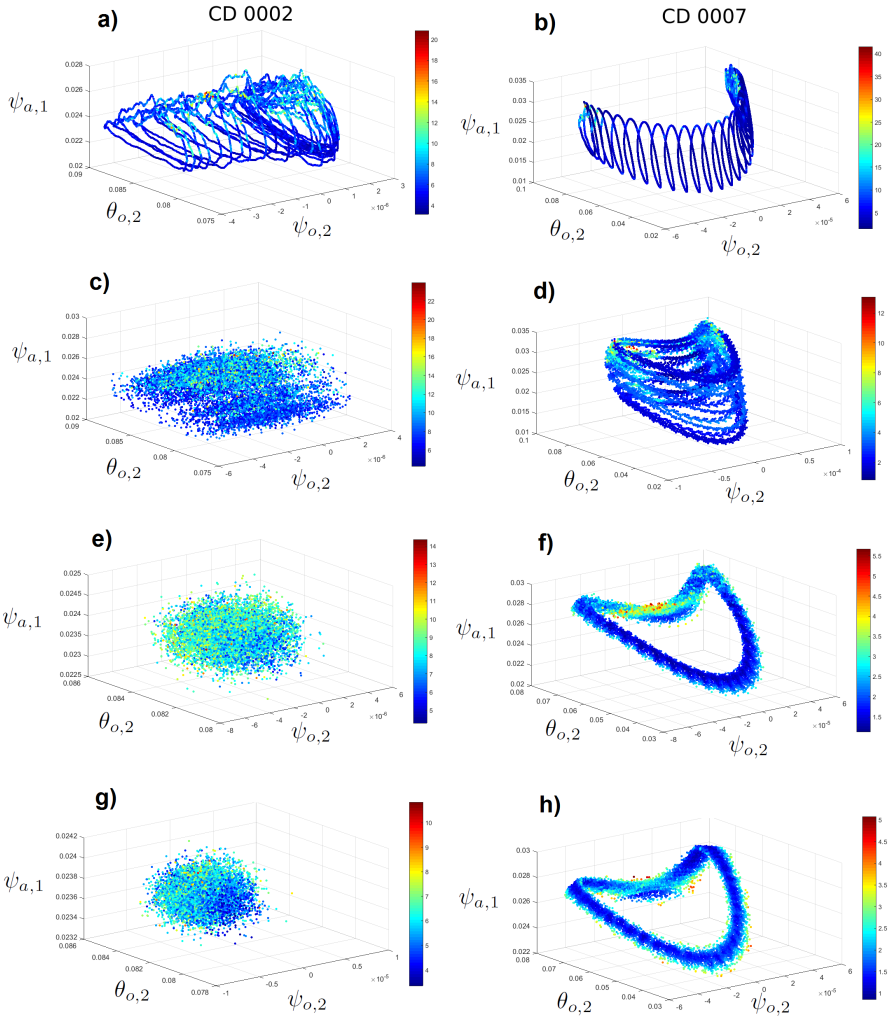

Figure 1. Poincaré sections for the modes 2,9,15. Different couplings a,c,e,g): C=0.002. b,d,f,h) C=0.007. Different averaging windows: a,b) daily; c,d) monthly; e,f) yearly; g,h) 8 years averages.

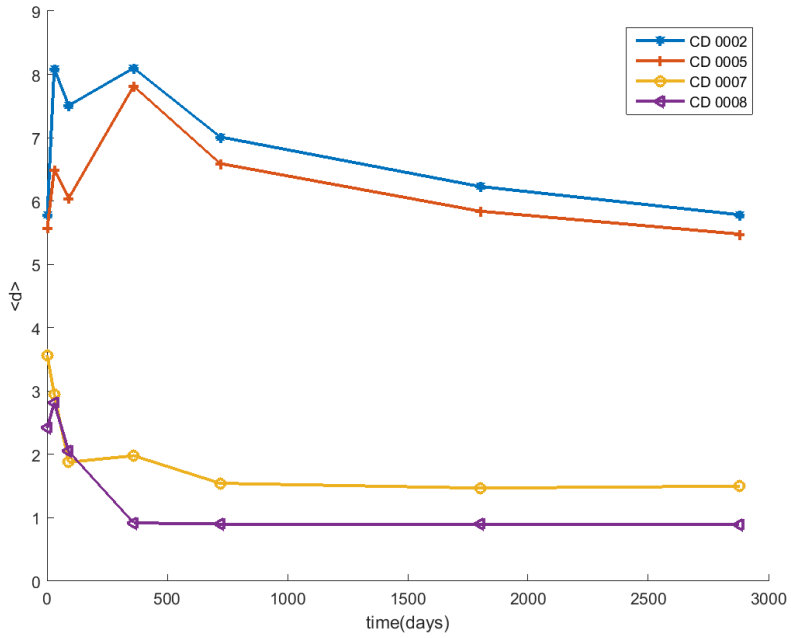

Figure 2. Average local dimensions as a function of the coupling and the averaging window.

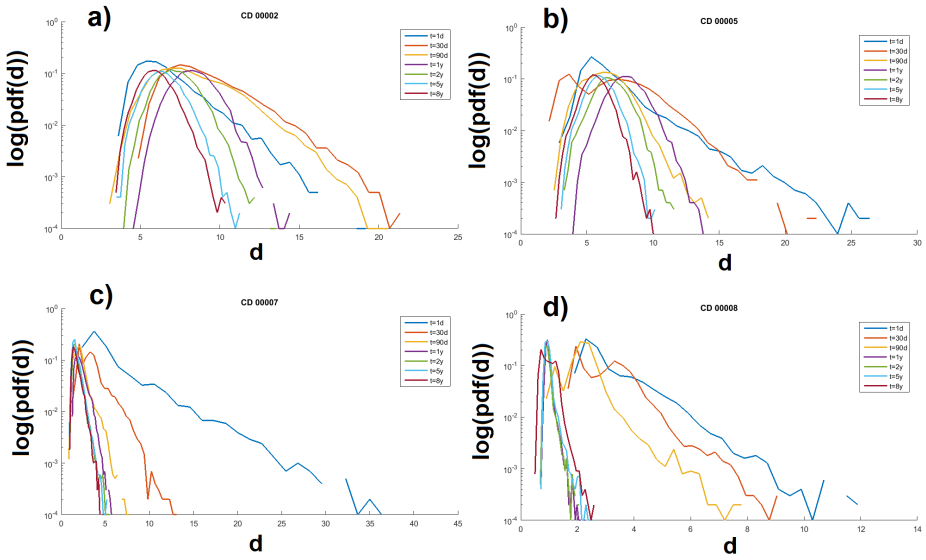

Figure 3. Attractor dimensions' distributions as a function of the coupling and the averaging window. a) C=0.002, b) C=0.005, c) C=0.007, d) C=0.008

.

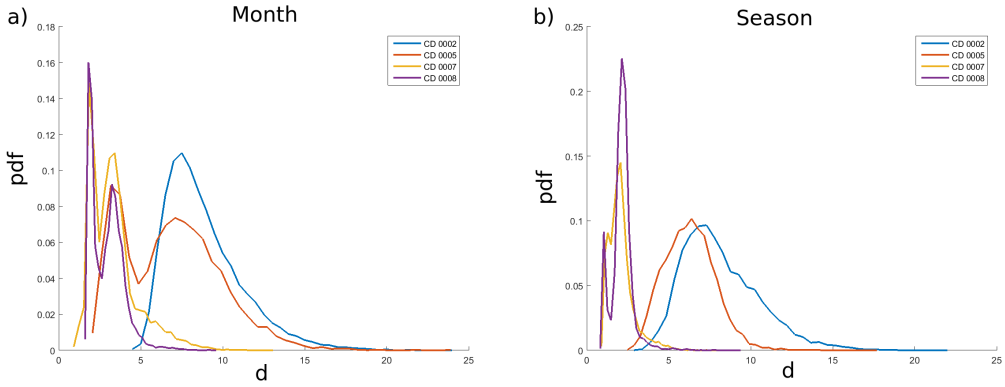

Figure 4. Attractor dimensions' distributions as a function of the coupling for monthly (a) and seasonal (b) averaging time.

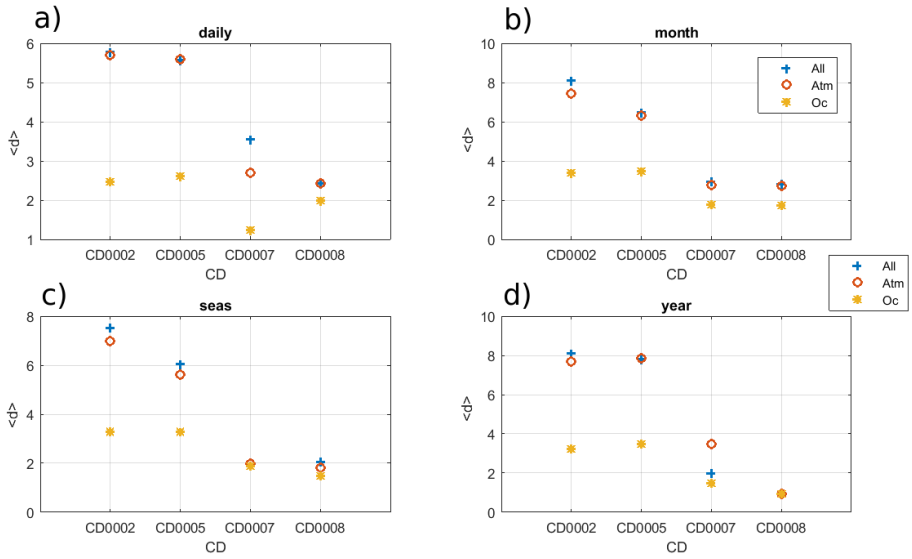

Figure 5. Average dimensions $\langle d \rangle$ computed selecting all modes (blue stars) atmospheric modes only (red crosses), oceanic modes only (yellow triangles). a) daily, b) monthly, c) seasonal and d) yearly data.

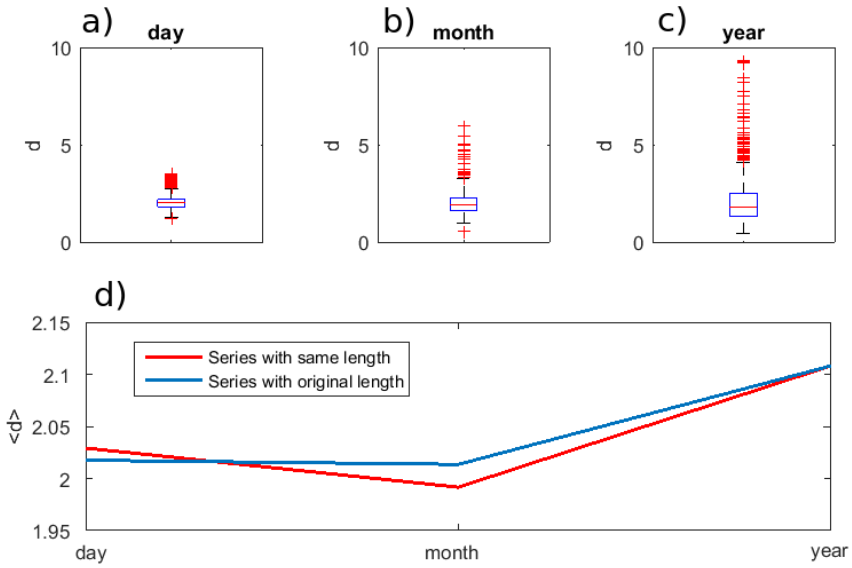

Figure 6. a,b,c): boxplots of local dimensions d for NAO and Nino3 indices at different time scales. On each box, the central mark is the median, the edges of the box are the 25th and 75th percentiles, the whiskers extend to the most extreme data points not considered outliers, and outliers are plotted individually. a) daily, b) monthly and c) yearly data. d): average dimension $\langle d \rangle$ computed with the full length time-series (blue) and only 947 time steps (red).